LANGMUIR Article
Cite This: Langmuir 2018, 34, 9774−9780
pubs.acs.org/Langmuir

White and Tunable Emission from and Rhodamine B Detection by Modified Zinc Oxide Nanowalls

Jung-Soo Kang,[†] A-Ri Ham,[‡] Jun-Gill Kang,[‡,§] and Kam Tong Leung*[,†]

[†]WATLab and Department of Chemistry, University of Waterloo, Waterloo, Ontario N2L 3G1, Canada
[‡]Department of Chemistry, Chungnam National University, Daejeon 34143, Republic of Korea
[§]ReSEAT Program, Korea Institute Science and Technology Information, Daejeon 34141, Republic of Korea

Supporting Information

ABSTRACT: To gain better optical and optoelectrical properties, doping trivalent lanthanide cations into host materials is a very attractive approach in nanoscience. Here, we use a transparent conducting oxide, zinc oxide, as the host material to directly embed trivalent terbium cations without the need for any postgrowth treatment, and we investigate the photophysical effect of the dopant. Trivalent Tb cations embedded in ZnO nanowalls produce hypersensitive green emission (at 545 nm, corresponding to the $^5D_4 \rightarrow {}^7F_5$ transition) and convert the emission color of ZnO from yellow into white. Evidently, the photoluminescence emission intensity of Tb(III) is further increased by close to 10-fold due to the plasmonic effect introduced by noble metal (Ag and Pt) nanoparticles. The characteristic Tb(III) emission is found to be tunable from white to red and is examined for its potential chemosensing application for rhodamine B involving a plausible cascade energy transfer mechanism from ZnO to rhodamine B via Tb(III) cations.

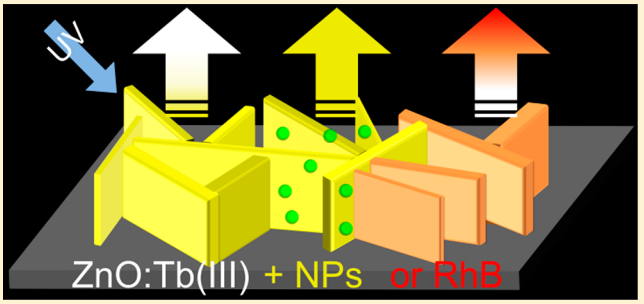

1. INTRODUCTION

ZnO nanostructures have received great interest for their applications in optoelectronics, piezotronics, spintronics, and photocatalysis because of their wide energy band gap (3.37 eV) and large exciton binding energy (~60 meV).[1−9] ZnO nanostructures exhibit two emission bands: a sharp deep UV emission associated with the excitonic band edge and a broad visible emission attributable to various intrinsic defects.[10−12] These unique optical properties have made ZnO nanostructures one of the most promising materials for next-generation optoelectronic devices operating in the UV or visible region.[13−17]

Doping of trivalent rare earth (RE) transition metal ions into ZnO nanostructures has been conducted with the goal to improve their intrinsic physical properties, such as optical, electronic, and magnetic properties.[18−30] They are particularly attractive for potential application in visible optoelectronics because of their unique luminescence properties, such as hypersensitivity to the environment, narrow bandwidth, and long lifetime in the millisecond range.[22−33] Among the RE(III) ions, europium and terbium are found to emit red and green luminescence, respectively. To date, most studies have focused on Eu(III)-doped ZnO nanostructures.[23−28] Because the optical application of RE(III)-doped ZnO nanostructures relies on the energy transfer from ZnO to RE(III), Eu(III) is less effective than Tb(III) due to the larger energy difference between the conduction band minimum of ZnO and the emitting level for Eu(III) ($^5D_0$) than that for Tb(III) ($^5D_4$). Recently, Tb(III)-doped ZnO [ZnO:Tb(III)] nanostructured materials, such as nanorods, nanoparticles, nanocrystals, and microspheres, have been prepared by a number of methods including pulsed laser deposition and sol−gel and hydrothermal syntheses.[19,28,34−37] The resulting ZnO:Tb(III) nanostructures, however, were found to produce very weak lines as no or only trace characteristic emission originated from Tb(III) was observed. The low emission intensities did not improve even with additional postannealing of the ZnO:Tb(III) nanostructures.

In this study, ZnO:Tb(III) nanowalls are electrochemically grown on indium−tin oxide (ITO) coated glass. Upon excitation by UV light, the as-grown ZnO:Tb(III) nanowalls are found to produce a series of sharp lines superpositioned on the green emission from the intrinsic defects, and the photophysical properties of these ZnO:Tb(III) nanowalls on an ITO-glass substrate are characterized in detail. We further investigate how the photoluminescence (PL) properties of these ZnO:Tb(III) nanowalls are affected by surface modification with noble metal nanoparticles (NPs) and organic chromophores. To date, the PL enhancement of ZnO due to localized surface plasmon resonances (LSPRs) of metal nanoparticles has been realized only from ZnO films treated with metal NPs involving elaborate, complex

Received: April 14, 2018
Revised: May 22, 2018
Published: July 27, 2018

DOI: 10.1021/acs.langmuir.8b01238
Langmuir 2018, 34, 9774−9780

fabrication methods, such as electron-beam lithography, ion implantation, and atomic layer deposition.[38−41] In contrast, ZnO nanorods and nanocrystals treated with simple surface modification by metal NPs have thus far not been found to exhibit LSPR in the UV and visible luminescence.[42−45] Here, we deposit NPs of noble metals (Ag, Pt, and Au) of a few nanometers in size by a simple dip-casting method and demonstrate the remarkable enhancement of the Tb(III) green emission by Ag NPs. In addition, the feasibility of using the Tb-related green emission as a fluorescence probe is examined by surface modification using appropriate organic materials. As a model chromophore that absorbs green light, Rhodamine B (RhB) produces moderate fluorescence intensity in ethanol or aqueous solutions, while its fluorescence intensity is very weak to none in powder form or in thin film (drop-casted on the substrate). We show that the RhB/ZnO:Tb(III) nanowall heterostructures exhibit substantial emission in the orange-red region, demonstrating its potential use as a fluorescence-based chemosensor.

2. RESULTS AND DISCUSSION

The scanning electron microscopy (SEM) images of pristine and Tb-doped ZnO nanowalls obtained with various Tb(III) concentrations are shown in Figure 1. Undoped ZnO

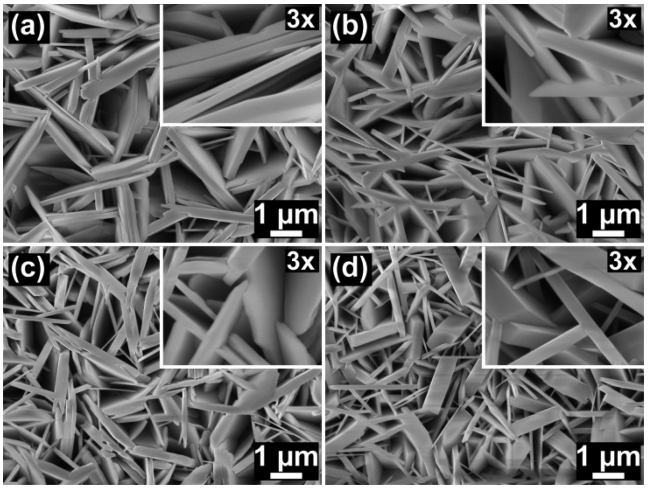

Figure 1. SEM images of (a) pristine ZnO nanowalls and Tb-doped ZnO nanowalls obtained with Tb(III) concentrations of (b) 1, (c) 5, and (d) 10 mM.

nanowalls appear to be 100−200 nm thick (Figure 1a). Although the thickness of (Tb-doped) ZnO nanowalls has not changed upon introduction of Tb(III), the surface of the nanowalls has evidently become smoother (Figure 1b,c). As the concentration of Tb(III) reaches 10 mM, the nanowalls tend to stack together to form thicker nanowalls (with average thickness of 700−800 nm), and nanowalls with a wider thickness distribution are observed (Figure 1d).

To confirm the uniformity of Tb(III) cation distribution in the ZnO nanowalls, composition analysis by scanning auger microscopy (SAM) and X-ray photoelectron spectroscopy (XPS) as a function of Ar^+ ion sputtering time has been performed. Because the SAM system employs an electron beam with a small beam spot and it is capable of a high spatial resolution of ∼20 nm, we collect Auger electron spectra at three well-separated locations of the nanowall sample as marked on the SEM image (Figure 2a). Because of the small

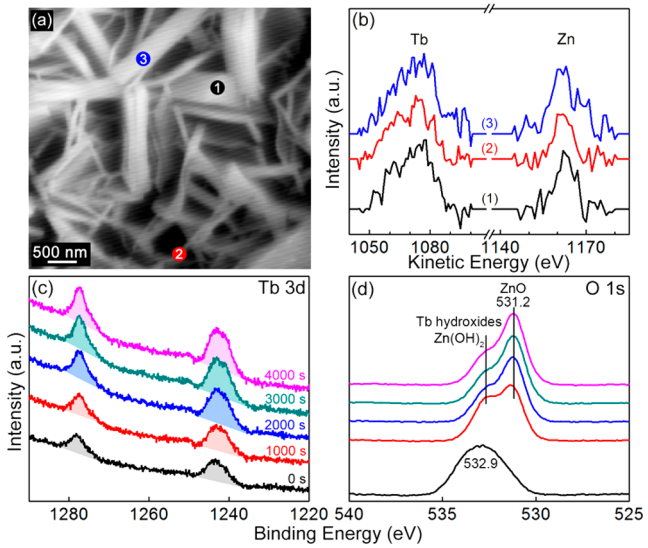

Figure 2. (a) SEM image and (b) background-subtracted Auger electron spectra collected at three different locations marked in (a) for as-deposited Tb-doped ZnO nanowalls obtained with a Tb(III) concentration of 10 mM. XPS spectra of (c) Tb 3d and (d) O 1s regions for as-grown Tb-doped ZnO nanowalls and upon sputtering for 1000, 2000, 3000, and 4000 s.

amount of trivalent Tb cation dopants, we have removed the spectral background to better illustrate the Tb peaks. Evidently, the nearly identical Tb MNN Auger intensities found at three different sites confirm that the Tb(III) dopant surface composition is independent of the size of the nanowalls and it appears uniform for the entire sample.[46] Figures 2c and 2d show the XPS spectra of the Tb 3d and O 1s regions, respectively. Both position and intensity of the Tb $3d_{5/2}$ ($3d_{3/2}$) peak found at 1242.4 eV (1277.5 eV) remain unchanged with Ar^+ sputtering, which indicates excellent doping uniformity of Tb(III) throughout the ZnO nanowalls. The broad O 1s peak at 532.9 eV can be attributed to $Zn(OH)_2$ and/or Tb hydroxides on the surface of the nanowalls for the as-grown sample. Upon Ar^+ sputtering, a new O 1s peak at 531.2 eV corresponding to ZnO emerges, and it becomes more prominent. The spectral evolution of the observed O 1s spectra confirms that the ZnO:Tb(III) nanowalls follow the well-known growth mechanism of electrochemically deposited ZnO nanostructures.[23] In addition, semiquantitative analysis of ZnO:Tb(III) nanowalls using XPS survey spectra reveals that the concentration of Tb(III) is ∼1.5 at. % for ZnO:Tb nanowalls obtained with a Tb(III) concentration of 10 mM. Figure S1 shows the transmission electron microscopy (TEM) image of a ZnO:Tb(III) nanowall sample obtained with a Tb(III) concentration of 10 mM. The corresponding high-resolution TEM image (Figure S1, inset) reveals a lattice spacing of 2.8 Å, in good accord with the interplanar spacing of ZnO(100) planes.

Figure 3a shows the PL spectra of ZnO:Tb(III) nanowalls on ITO-glass obtained in electrolytes with three different Tb(III) concentrations. For nanowalls grown from the electrolyte with 1 mM Tb(III) solution, excitation at 325 nm produces the characteristic emission from the as-grown ZnO nanostructures, with the near-band-edge emission peak at 375 nm and the broad defect-related emission band spanning over the visible region. No additional bands arisen from the Tb(III) dopants are observed from these doped nanowalls. However,

DOI: 10.1021/acs.langmuir.8b01238
Langmuir 2018, 34, 9774−9780

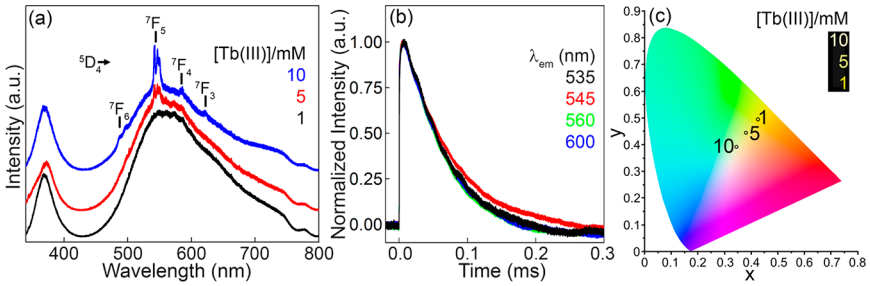

Figure 3. (a) PL spectra (λ_{ex} = 325 nm) of Tb-doped ZnO nanowalls obtained in an electrolyte with a Zn^{2+} concentration of 0.1 M along with 1, 5, and 10 mM Tb(III) concentration. (b) Time profiles of the visible emissions (λ_{ex} = 337.1 nm) at 535, 545, 560, and 600 nm from Tb-doped ZnO nanowalls obtained with a 10 mM Tb(III) concentration. (c) CIE chromaticity diagram depicting the color coordinates of ZnO:Tb(III) nanowalls obtained with 1, 5, and 10 mM Tb(III) concentration.

the PL spectrum for doped nanowalls grown with the electrolyte containing 5 mM Tb(III) solution exhibits additional well-defined sharp peaks in the green region superpositioned on the defect-related broad band. When the Tb(III) concentration reaches 10 mM, sharp characteristic emission lines from Tb(III) evidently appear with barycenters at 489, 545, 582, and 621 nm. These bands correspond to the transitions from the $^5D_4$ state to the $^7F_{6,5,4,3}$ states, respectively.

Among these emission lines, the $^5D_4 \rightarrow {}^7F_5$ transition at 545 nm corresponds to the most intense luminescence, and it exhibits a series of sharp features, as evidenced from the splitting arising from the $(2J + 1)$ degeneracy. The excitation spectra for the 545 nm emission have been measured at several temperatures (10, 70, 150, and 300 K). Figure S2 shows that except for the intensity increasing inversely with the temperature, there is generally no significant difference in the band structure. The position of the band maximum for the room-temperature spectrum appears to be slightly red-shifted compared to those for the spectra measured at lower temperatures. The broad band with band maximum at 355 nm and no sharp feature spanning over the 300−380 nm region in these lower-temperature spectra is very similar to those of the near-band-edge emission from ZnO nanowalls (Figure S2). In general, direct excitation for the 545 nm emission from Tb(III) is expected to produce a series of sharp lines with moderate intensities in the 300−400 nm region, corresponding to the transitions from the $^5F_6$ state to the $^5G_{6,5}$ and $^5L_{10,9}$ states.[47] As these lines are evidently not observed in the broad excitation band, this indicates that the emission from Tb(III) can only be realized by energy transfer from ZnO.

The time profiles of the emission decay from ZnO:Tb(III) nanowalls obtained with a 10 mM Tb(III) concentration have been measured to examine the energy transfer dynamics. The lifetime (τ) of the ZnO band-edge emission has been reported to be highly dependent on its morphology: τ = 112 ps for the bulk single-crystal sample, τ = 37 ps for the nanosphere, and τ = 8 ps for the nanowire.[48] The lifetime of the observed visible emission ($\tau \approx 4.5$ ps) is evidently much shorter than any of the reported band-edge emissions of ZnO nanostructures. Figure 3b shows the time profiles of the PL intensities of the visible emission at λ_{em} = 535, 545, 560, and 600 nm from the ZnO:Tb(III) nanowalls pumped by a 337.1 nm N_2 laser with a 0.03 ms pulse width. The time profile of the 545 nm emission is discernibly different from those of the other emissions, with the decay of the 545 nm emission being notably slower (i.e., with a larger τ) than those of the other emissions. Assuming that the lifetime of the visible emission from the defects is in the picosecond range, the wavelength-independent time profiles (i.e., those obtained with λ_{em} = 535, 560, and 600 nm) should originate from the scattered light of the excitation laser, the decay lifetime of which has been estimated to be τ_{scatt} = 67.4 μs. The observed time evolution intensity of the 545 nm emission can therefore be considered to consist of two decay components: one for the scattered light and one for the emission from Tb(III). As shown in Figure S3, the time profile can indeed be fitted with two exponential components of τ_{scatt} = 67.4 μs (87%) and τ_{Tb} = 150 μs (13%), with an excellent R^2 value (>0.999). The quantum yield of the sensitized luminescence of Tb(III) can be estimated by using the relationship between the observed lifetime of Tb(III) (τ_{Tb}) and its natural lifetime (τ_0).[49] Using the reported value of 4.75 ms for τ_0 of Tb(III), we obtain a quantum yield for the sensitized emission from Tb(III) to be 0.032.[45]

To clearly observe the effect of the Tb(III) cation on the luminescence properties, we perform color chromaticity measurement on undoped and Tb(III) doped ZnO nanowalls, and we illustrate the results in a Commission Internationale de L'Eclairage (CIE) color diagram shown in Figure 3c. The CIE x, y color coordinates and the emission colors of undoped ZnO and ZnO:Tb(III) samples are summarized in Table S1. These are significant results because they show that the emission color of ZnO:Tb(III) is tunable by adjusting the Tb(III) cation concentration. The color coordinates of undoped ZnO and ZnO:Tb(III) with 1 mM Tb(III) cation concentration show minimal difference between each other. When the Tb(III) cation concentration reaches 5 mM, the emission color changes to light yellow. With increasing Tb(III) cation concentration to 10 mM, the emission color moves toward blue and changes to white with a hint of light green. Because the CIE color coordinates of ZnO:Tb(III) obtained with a 10 mM Tb(III) cation concentration are (0.349, 0.388) and are located nearby various white coordinate points of standard illuminants, as-grown ZnO:Tb(III) with a 10 mM Tb(III) cation concentration can therefore be considered as a white light source.

We also investigate LSPR on the luminescence of the ZnO:Tb(III) nanowalls (supported on ITO-glass) that are decorated with NPs of three different noble metals: Ag, Pt, and Au. The deposition of the NPs has been performed by simple dip-casting. The amount of the deposited NPs could be increased by increasing the number of dip-casting cycles. The PL spectra so obtained are resolved into two types of emission components: sharp Tb(III)-related emission features and broad ZnO-related emission bands. Figure 4a shows the plasmonic effects of Ag, Pt, and Au NPs on the emission spectra of the ZnO:Tb(III) nanowalls obtained with a 10 mM

DOI: 10.1021/acs.langmuir.8b01238
Langmuir 2018, 34, 9774−9780

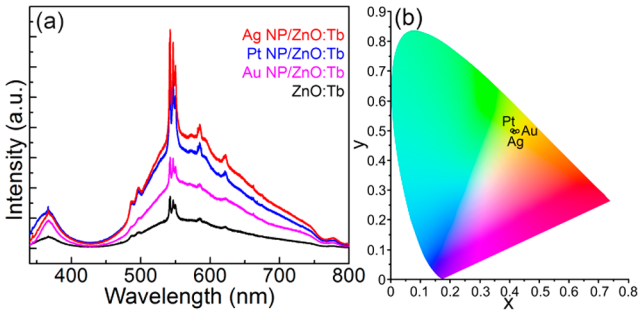

Figure 4. (a) PL spectra (λ_{ex} = 325 nm) of Tb-doped ZnO nanowalls decorated with the optimal amounts of Ag, Pt, and Au NPs to provide the maximal LSPR effect. (b) CIE chromaticity diagram depicting the color coordinates of surface-modified ZnO:Tb(III) nanowalls with optimized amounts of Ag, Pt, and Au NPs.

Tb(III) cation concentration. (The emission spectra are obtained with the excitation wavelength set at 325 nm.) For Ag NPs, the relative intensities of the broad ZnO near-band-edge emission band at 369 nm and the sharp Tb(III) $^5D_4 \rightarrow {}^7F_5$ peak at 545 nm are not affected by the first three dip-casting cycles, after which the relative band intensities of the two emission features increase with increasing number of dip-casting cycles. After eight dip-casting cycles, the enhancement of the two emission features has reached a maximum. Relative to the undecorated ZnO:Tb(III) nanowalls, the Tb(III) $^5D_4 \rightarrow {}^7F_5$ emission peak and the ZnO band-edge emission band of the NP-decorated ZnO:Tb(III) nanowalls are found to increase in intensity by approximately 10-fold and 6-fold, respectively. Because the energy transfer from the ZnO band-edge emission (donor) to intrinsic defects and that to Tb(III) are competing with each other, this suggests that as acceptors in the energy-transfer processes the Tb(III) dopants could be significantly more effective than the intrinsic defects of ZnO. The LSPR enhancement introduced by the Pt NPs is evidently less than that by the Ag NPs. For the Pt NPs, five dip-casting cycles produce the maximum LSPR enhancement on both emission components, with more than 6-fold and 3-fold increases for the respective Tb(III) and ZnO-related emission bands. Surprisingly, the Au NPs do not appear to enhance the emission from the Tb-doped ZnO nanowalls significantly. This is better illustrated in Figure S4, which compares the PL emission lines of the undecorated sample and the NP-decorated ZnO:Tb(III) nanowall samples that give the maximal intensities, after removing the underlying broad-band intensities.

To review the LSPR effect on the emission color, we have also conducted color chromaticity measurement on ZnO:Tb-(III) nanowalls obtained with a 10 mM Tb(III) cation concentration and optimized amounts of Ag, Pt, and Au NPs, and the result is shown in Figure 4b. With the introduction of NPs, the emission colors revert back to those of undoped ZnO nanowalls and ZnO:Tb(III) nanowalls obtained with a 1 mM Tb(III) cation concentration. Because the emission of ZnO defects are broad and its intensity is also largely enhanced by LSPR, emission from the undoped ZnO (or ZnO:Tb(III) with a 1 mM Tb(III) cation concentration) nanowall sample dominates the color of ZnO:Tb(III) emission regardless of the degree of LSPR enhancement and the concentration of Tb(III) cations.

To evaluate the potential use of ZnO:Tb(III) nanowalls as a fluorescence-based chemosensor, we measure the PL spectra of the ZnO:Tb(III) nanowalls treated with sequential applications of 1 and 3 drops of 10 mM RhB solution in CH_2Cl_2. As shown in the Figure S5, the absorption peak of RhB solution appears to coincide with green emission lines of Tb(III) cations, and this enables the energy transfer from Tb(III) to RhB. Figure 5a compares the PL spectra of these RhB/

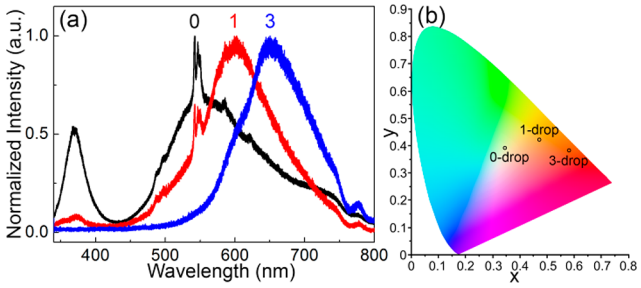

Figure 5. (a) Emission spectra (λ_{ex} = 325 nm) of Tb-doped ZnO nanowalls without and with 1 and 3 drops of RhB treatment. These spectra have been normalized at their respective maximum band intensities. (b) CIE chromaticity diagram depicting the color coordinates of ZnO:Tb(III) nanowalls with 0-, 1-, and 3-drop RhB.

ZnO:Tb(III) nanowall heterostructures with that of untreated ZnO:Tb(III) nanowalls, all obtained with the excitation wavelength set at 325 nm. To clarify the effect of RhB, PL spectra were normalized by their maximum intensities (to expose the relative changes in the spectral profile). The one-drop RhB treatment has evidently caused the visible emission band maximum to shift from 550 to 603 nm, and it also results in reduction in the intensity of the Tb(III) green emission at 545 nm. This red-shift is even more apparent for the ZnO:Tb(III) nanowalls treated with three drops of RhB, with the band maximum now located at 653 nm along with a weak shoulder at 600 nm and the Tb(III) lines totally quenched. For comparison purposes, additional experiments of RhB functionalization on undoped ZnO nanowalls were performed and are shown in Figure S6. With excitation at 325 nm, there is no difference of sensitized luminescence of RhB between ZnO:Tb(III) and undoped ZnO. However, the energy transfer efficiency from the Tb(III)-doped nanowalls to RhB is significantly different from that from undoped nanowalls to RhB. Specifically, ZnO:Tb(III) (with an efficiency of 89%) shows more than 7 times higher than undoped ZnO (12%), which indicates that ZnO:Tb(III) is a promising candidate for sensing RhB or other dyes with a similar excitation range. In a separate experiment, a RhB thin film is deposited on a quartz substrate, and excitation at 325 nm of this sample does not produce any emission from the RhB film.

The emission colors of RhB/ZnO:Tb(III) are measured and shown in Figure 5b. The color measurement result follows a similar trend as that of the PL results. The initial single drop of RhB changes the color from white to light orange, and the color becomes orangish-red with additional drops of RhB. In combination with results from other color measurements, ZnO:Tb(III) therefore demonstrates its unique capability to tune the emission color by adjusting the Tb(III) cation concentration and by varying the amount of fluorescent dyes.

To account for the observed spectral changes on Tb-doped ZnO nanowalls induced by RhB, we propose a dopant-mediated energy transfer mechanism. Figures 6a and 6c illustrate respectively our energy transfer model and the

DOI: 10.1021/acs.langmuir.8b01238
Langmuir 2018, 34, 9774−9780

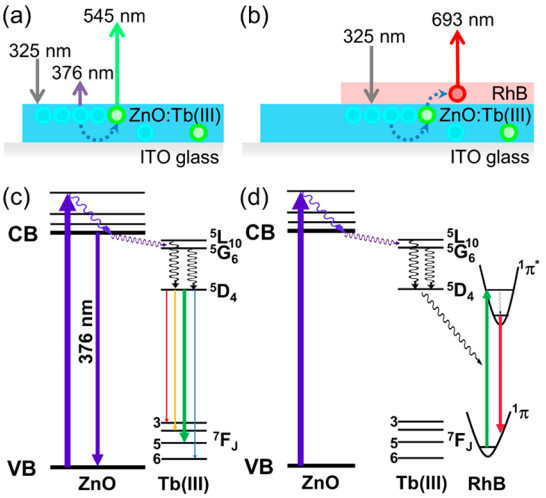

Figure 6. Energy transfer models and energy-level diagrams illustrating the proposed energy transfer mechanisms for (a, c) ZnO:Tb(III) nanowalls, in which energy transfer occurs between ZnO nanowalls and the dopant Tb(III), resulting in the ZnO near-band-edge emission (at 376 nm) and several characteristic Tb(III) emissions in the visible range, and (b, d) ZnO:Tb(III) nanowalls and Rhodamine B (RhB), in which a second energy transfer between the Tb(III) and RhB that leads to the red emission.

energy-level scheme responsible for the sensitized emission from Tb(III) via an energy transfer mechanism. Taking into account the resonance energy transfer, the $^5L_{10}$ state at 27100 cm^{-1} (3.36 eV) and $^5G_6$ state at 26500 cm^{-1} (3.29 eV) of Tb(III) play a key role in receiving the energy from the ZnO nanostructures because these two states lie just below the conduction band (CB) of ZnO.[47] The energy transfer is initialized by the excitation of ZnO from the valence band (VB) to the upper levels in the conduction band, followed by the subsequent relaxation from the upper levels to the lowest level in the conduction band. Two optical de-excitation processes could take place competitively from the lowest conduction band level: (a) direct radiative transition to the valence band with $\lambda_{em} \approx 376$ nm (i.e., the ZnO band-edge emission) and (b) energy transfers to the dopant Tb(III) via the $^5L_{10}$ and $^5G_6$ states (Figure 6c) and to the intrinsic defects localized near the conduction band (not shown). In the ZnO:Tb(III) nanowalls, the energy transfer is evidently more effective than the radiative transition because the visible Tb(III) emissions and the ZnO defect-related emissions are much stronger than the 376 nm emission. The subsequent relaxation from the receiving $^5L_{10}$ and $^5G_6$ states to the emitting $^5D_4$ state at 20500 cm^{-1} (2.04 eV) then leads to a series of sharp emission lines from the Tb(III) $^5D_4$ state to the ^7F_J (J = 6, 5, 4, 3) states that span over the 480−640 nm region (as observed in Figure 4a).

For the RhB/ZnO:Tb(III) hybrid heterostructure (Figures 6b and 6d), the red emission from RhB is generated by further efficient energy transfer from the ZnO:Tb(III) nanowalls. In the Förster theory, the energy-transfer efficiency is governed by not only the spectral overlap between the donor emission spectrum and the acceptor excitation spectrum but also the separation between the donor and the acceptor. The maximum separation over which the Förster energy transfer can take place is typically 30−50 Å. For the hybrid structure, there is essentially no gap between the donor layer and the acceptor layer so that the energy transfer could take place very efficiently. A cascading energy-transfer model is proposed for the red emission from the hybrid structure. As shown in Figure 6c, the population of the $^5D_4$ state of Tb(III) is enhanced via the energy transfer from the ZnO conduction band to Tb(III). The 545 nm emission (from the $^5D_4$ state to the $^7F_5$ state, one of the ^7F_J states) of Tb(III) coincides with the excitation from the $^1\pi$ ground state to the $^1\pi^*$ excited state of RhB. For the hybrid structure, the cascade energy transfer originates from the conduction band of ZnO to the $^1\pi^*$ excited state of RhB, through the interface between the nanowall surface and the RhB layer via the $^5D_4$ state of the Tb(III) dopant (acting as the intermediate "cascade" state) by this second nonradiative energy transfer. Subsequent relaxation from the $^1\pi^*$ vibronic states followed by the radiative transitions to one of the $^1\pi$ vibronic states then leads to the red emission.

3. CONCLUSION

We have successfully synthesized Tb-doped ZnO nanowalls using a facile electrochemical deposition method. The SEM data show that the concentration of Tb(III) ions could affect the thickness of the as-grown Tb-doped ZnO nanowalls. Depth-profiling O 1s and Tb 3d XPS spectra confirm that Tb is uniformly distributed throughout the ZnO nanowalls. PL measurement shows that the strong sharp Tb(III) green emission lines are superposed on the ZnO defect-related emission band via energy transfer from ZnO to Tb(III) (Figure 6c). Our CIE color chromaticity measurements of ZnO:Tb(III) further demonstrate tunable emission of ZnO:Tb(III) as a function of Tb(III) concentration and show that white emission can be obtained with a 10 mM Tb(III) concentration. The sensitized emission from Tb(III) is remarkably responsive to the LSPRs of Ag and Pt nanoparticles (but surprisingly not significantly to Au nanoparticles) compared with the band-edge and the defect-related emissions from the ZnO nanostructures. Furthermore, it is found that the enhanced green emission is very effective in sensitizing the fluorescence via the cascade energy transfer from the ZnO:Tb(III) nanowalls to the RhB dye through Tb(III), with Tb(III) serving as the cascade/interface between the nanowall and the dye layer in the hybrid dye/doped-nanowall structure (Figure 6d). This type of hybrid structures promises potential applications in the fluorescence-based probes, chemosensors, and tunable light sources.

■ ASSOCIATED CONTENT

Supporting Information

The Supporting Information is available free of charge on the ACS Publications website at DOI: 10.1021/acs.langmuir.8b01238.

Detailed experimental methods and additional data (Figures S1−S4 and Table S1) (PDF)

■ AUTHOR INFORMATION

Corresponding Author

*E-mail tong@uwaterloo.ca (K.T.L.).

ORCID

Kam Tong Leung: 0000-0002-1879-2806

Notes

The authors declare no competing financial interest.

DOI: 10.1021/acs.langmuir.8b01238
Langmuir 2018, 34, 9774−9780

■ ACKNOWLEDGMENTS

This work was supported by the Natural Sciences and Engineering Research Council of Canada.

■ REFERENCES

(1) Pradel, K. C.; Ding, Y.; Wu, W.; Bando, Y.; Fukata, N.; Wang, Z. L. Optoelectronic Properties of Solution Grown ZnO n-p or p-n Core−Shell Nanowire Arrays. *ACS Appl. Mater. Interfaces* **2016**, *8*, 4287−4291.

(2) Zhang, C.; Wang, X.; Chen, W.; Yang, J. An Analysis of The Extension of a ZnO Piezoelectric Semiconductor Nanofiber Under An Axial Force. *Smart Mater. Struct.* **2017**, *26*, 025030.

(3) Prestgard, M. C.; Siegel, G.; Roundy, R.; Raikh, M.; Tiwari, A. Temperature Dependence of The Spin Relaxation in Highly Degenerate ZnO Thin Films. *J. Appl. Phys.* **2015**, *117*, 083905.

(4) Wang, J.; Chen, R.; Xia, Y.; Wang, G.; Zhao, H.; Xiang, L.; Komarneni, S. Cost-effective Large-scale Synthesis of Oxygen-defective ZnO Photocatalyst With Superior Activities Under UV and Visible Light. *Ceram. Int.* **2017**, *43*, 1870−1879.

(5) Rousset, J.; Tsin, F.; Guc, M.; Vidal, J.; Le Bris, A.; Thomere, A.; Izquierdo-Roca, V.; Lincot, D. Perchlorate-Induced Doping of Electrodeposited ZnO Films for Optoelectronic Applications. *J. Phys. Chem. C* **2016**, *120*, 18953−18962.

(6) Su, Y. Q.; Zhu, Y.; Yong, D.; Chen, M.; Su, L.; Chen, A.; Wu, Y.; Pan, B.; Tang, Z. Enhanced Exciton Binding Energy of ZnO by Long-Distance Perturbation of Doped Be Atoms. *J. Phys. Chem. Lett.* **2016**, *7*, 1484−1489.

(7) Quan, Z.; Liu, X.; Qi, Y.; Song, Z.; Qi, S.; Zhou, G.; Xu, X. Robust Room Temperature Ferromagnetism and Band Gap Tuning in Nonmagnetic Mg Doped ZnO Films. *Appl. Surf. Sci.* **2017**, *399*, 751−757.

(8) Pradhan, D.; Leung, K. T. Vertical Growth of Two-Dimensional Zinc Oxide Nanostructures on ITO-Coated Glass: Effects of Deposition Temperature and Deposition Time. *J. Phys. Chem. C* **2008**, *112*, 1357−1364.

(9) Pradhan, D.; Sindhwani, S.; Leung, K. T. Parametric Study on Dimensional Control of ZnO Nanowalls and Nanowires by Electrochemical Deposition. *Nanoscale Res. Lett.* **2010**, *5*, 1727−1736.

(10) Fan, J.; Güell, F.; Fábrega, C.; Fairbrother, A.; Andreu, T.; López, A. M.; Morante, J. R.; Cabot, A. Visible Photoluminescence Components of Solution-Grown ZnO Nanowires: Influence of the Surface Depletion Layer. *J. Phys. Chem. C* **2012**, *116*, 19496−19502.

(11) Ahn, C. H.; Kim, Y. Y.; Kim, D. C.; Mohanta, S. K.; Cho, H. K. A Comparative Analysis of Deep Level Emission in ZnO Layers Deposited by Various Methods. *J. Appl. Phys.* **2009**, *105*, 013502.

(12) Tam, K. H.; Cheung, C. K.; Leung, Y. H.; Djurišić, A. B.; Ling, C. C.; Beling, C. D.; Fung, S.; Kwok, W. M.; Chan, W. K.; Phillips, D. L.; Ding, L.; Ge, W. K. Defects in ZnO Nanorods Prepared by a Hydrothermal Method. *J. Phys. Chem. B* **2006**, *110*, 20865−20871.

(13) Bao, R.; Wang, C.; Dong, L.; Yu, R.; Zhao, K.; Wang, Z. L.; Pan, C. Flexible and Controllable Piezo-Phototronic Pressure Mapping Sensor Matrix by ZnO NW/p-Polymer LED Array. *Adv. Funct. Mater.* **2015**, *25*, 2884−2891.

(14) Sathyaseelan, B.; Manikandan, E.; Sivakumar, K.; Kennedy, J.; Maaza, M. Enhanced Visible Photoluminescent and Structural Properties of ZnO/KIT-6 Nanoporous Materials for White Light Emitting Diode (w-LED) Application. *J. Alloys Compd.* **2015**, *651*, 479−482.

(15) Li, X.; Liang, R.; Tao, J.; Peng, Z.; Xu, Q.; Han, X.; Wang, X.; Wang, C.; Zhu, J.; Pan, C.; Wang, Z. L. Flexible Light Emission Diode Arrays Made of Transferred Si Microwires-ZnO Nanofilm with Piezo-Phototronic Effect Enhanced Lighting. *ACS Nano* **2017**, *11*, 3883−3889.

(16) Yang, L.; Liu, W.; Xu, H.; Ma, J.; Zhang, C.; Liu, C.; Wang, Z.; Liu, Y. Enhanced Near-UV Electroluminescence From p-GaN/i-Al_2O_3/n-ZnO Heterojunction LEDs by Optimizing The Insulator Thickness and Introducing Surface Plasmons of Ag Nanowires. *J. Mater. Chem. C* **2017**, *5*, 3288−3295.

(17) Hsu, C.-L.; Chang, L.-F.; Hsueh, T.-J. Light-activated Humidity and Gas Sensing by ZnO Nanowires Grown on LED at Room Temperature. *Sens. Actuators, B* **2017**, *249*, 265−277.

(18) Piao, J.; Tseng, L.-T.; Yi, J. Ferromagnetism in Sm Doped ZnO Nanorods by a Hydrothermal Method. *Chem. Phys. Lett.* **2016**, *649*, 19−22.

(19) Hastir, A.; Kohli, N.; Singh, R. C. Comparative Study on Gas Sensing Properties of Rare Earth (Tb, Dy and Er) Doped ZnO Sensor. *J. Phys. Chem. Solids* **2017**, *105*, 23−34.

(20) Azad, F.; Luo, C.; Su, S.; Younas, M.; Azeem, W.; Kuznetsov, A.; Azarov, A.; Shih, K.; Liao, C.; Maqsood, A.; Ling, F. C.-C. Surface Localization of The Er-related Optical Active Centers in Er Doped Zinc Oxide Films. *J. Appl. Phys.* **2017**, *121*, 235701.

(21) Franco, A., Jr.; Pessoni, H. V. S. Effect of Gd Doping on The Structural, Optical Band-gap, Dielectric and Magnetic Properties of ZnO Nanoparticles. *Physica B* **2017**, *506*, 145−151.

(22) Balestrieri, M.; Gallart, M.; Ziegler, M.; Bazylewski, P.; Ferblantier, G.; Schmerber, G.; Chang, G. S.; Gilliot, P.; Muller, D.; Slaoui, A.; Colis, S.; Dinia, A. Luminescent Properties and Energy Transfer in Pr^{3+} Doped and Pr^{3+}-Yb^{3+} Co-doped ZnO Thin Films. *J. Phys. Chem. C* **2014**, *118*, 13775−13780.

(23) Kang, J.-S.; Jeong, Y.-K.; Kang, J.-G.; Zhao, L.; Sohn, Y.; Pradhan, D.; Leung, K. T. Observation of Mediated Cascade Energy Transfer in Europium-Doped ZnO Nanowalls by 1,10-Phenanthroline. *J. Phys. Chem. C* **2015**, *119*, 2142−2147.

(24) Lorke, M.; Frauenheim, T.; da Rosa, A. L. Many-body Electronic Structure Calculations of Eu-doped ZnO. *Phys. Rev. B: Condens. Matter Mater. Phys.* **2016**, *93*, 115132.

(25) Senapati, S.; Nanda, K. K. Designing Dual Emissions via Co-doping or Physical Mixing of Individually Doped ZnO and Their Implications in Optical Thermometry. *ACS Appl. Mater. Interfaces* **2017**, *9*, 16305−16312.

(26) Zhou, R.; Zhao, Q.; Liu, K.-K.; Lu, Y.-J.; Dong, L.; Shan, C.-X. Europium-decorated ZnO Quantum Dots as A Fluorescent Sensor for The Detection of An Anthrax Biomarker. *J. Mater. Chem. C* **2017**, *5*, 1685−1691.

(27) Dhara, S.; Raychaudhuri, A. K. Enhancement in Red Emission at Room Temperature from Europium Doped ZnO Nanowires by 1,10 Phenanthroline-europium Interface Induced Resonant Excitations. *AIP Adv.* **2017**, *7*, 025306.

(28) Hastir, A.; Opila, R. L.; Kohli, N.; Onuk, Z.; Yuan, B.; Jones, K.; Virpal; Singh, R. C. Deposition, Characterization and Gas Sensors Application of RF Magnetron-sputtered Terbium-doped ZnO Films. *J. Mater. Sci.* **2017**, *52*, 8502−8517.

(29) Abbass, A. E.; Swart, H. C.; Kroon, R. E. Use of ZnO:Tb Down-conversion Phosphor for Ag Nanoparticle Plasmon Absorption Using a He-Cd Ultraviolet Laser. *Luminescence* **2016**, *31*, 1182−1186.

(30) Rani, S.; Lal, B.; Saxena, S.; Shukla, S. Excitation Dependence of The Photoluminescence of ZnO: Tb Nanophosphor. *AIP Conf. Proc.* **2016**, *1860*, 020006.

(31) Kang, J.-S.; Leung, K. T.; Cho, H.-K.; Kang, J.-G.; Sohn, Y. Luminescence and Magnetic Properties of Tb(III) Complexes with TETA and Synergistic Effect by 1,10-Phenanthroline. *B. Kor. Chem. Soc.* **2016**, *37*, 1458−1463.

(32) Kang, J.-S.; Leung, K. T.; Nah, M.-K.; Shin, J.-S.; Kang, M.-H.; Shong, B.; Kang, J.-G.; Lee, J.; Sohn, Y. Neighbour-sensitized Near-infrared Emission of New Nd(III) and Er(III) Complexes with 1-(anthracene-2-yl)-4,4,4-trifluoro-1,3-butanedione. *New J. Chem.* **2016**, *40*, 9702−9710.

(33) Kang, J.-S.; Jeong, Y.-K.; Shim, Y. S.; Rout, S.; Leung, K. T.; Sohn, Y.; Kang, J.-G. Structures, and Luminescence and Magnetic Properties of Ln(III) Complexes Bearing Dibenzoylmethane Ligand (Ln = Eu and Gd). *J. Lumin.* **2016**, *178*, 368−374.

(34) Layek, A.; Banerjee, S.; Manna, B.; Chowdhury, A. Synthesis of Rare-earth Doped ZnO Nanorods and Their Defect−dopant Correlated Enhanced Visible-orange Luminescence. *RSC Adv.* **2016**, *6*, 35892−35900.

DOI: 10.1021/acs.langmuir.8b01238
Langmuir 2018, 34, 9774−9780

(35) Sharma, A.; Dhar, S.; Singh, B. P.; Kundu, T.; Spasova, M.; Farle, M. Influence of Tb Doping on the Luminescence Characteristics of ZnO Nanoparticles. *J. Nanopart. Res.* **2012**, *14*, 676.
(36) Jin, N.; Li, H.; Liu, F.; Xie, Y.-H. Microstructure and Luminescence Properties of Tb^{3+} Doped ZnO Quantum Dots. *J. Nanosci. Nanotechnol.* **2016**, *16*, 3592−3596.
(37) Kumar, V.; Ntwaeaborwa, O. M.; Swart, H. C. Deep Level Defect Correlated Emission and Si Diffusion in ZnO:Tb^{3+} Thin Films Prepared by Pulsed Laser Deposition. *J. Colloid Interface Sci.* **2016**, *465*, 295−303.
(38) Gogurla, N.; Sinha, A. K.; Santra, S.; Manna, S.; Ray, S. K. Multifunctional Au-ZnO Plasmonic Nanostructures for Enhanced UV Photodetector and Room Temperature NO Sensing Devices. *Sci. Rep.* **2015**, *4*, 6483.
(39) Lin, Y.; Liu, X. Q.; Wang, T.; Chen, C.; Wu, H.; Liao, L.; Liu, C. Shape-Dependent Localized Surface Plasmon Enhanced UV-Emission from ZnO Grown by Atomic Layer Deposition. *Nanotechnology* **2013**, *24*, 125705.
(40) Ko, C.-T.; Han, Y.-Y.; Chen, C.-H.; Shieh, J.; Chen, M.-J. Enormous Plasmonic Enhancement and Suppressed Quenching of Luminescence from Nanoscale ZnO Films by Uniformly Dispersed Atomic-Layer-Deposited Platinum with Optimized Spacer Thickness. *J. Phys. Chem. C* **2013**, *117*, 26204−26212.
(41) Xiao, X. H.; Ren, F.; Zhou, X. D.; Peng, T. C.; Wu, W.; Peng, X. N.; Yu, X. F.; Jiang, C. Z. Surface Plasmon-Enhanced Light Emission Using Silver Nanoparticles Embedded in ZnO. *Appl. Phys. Lett.* **2010**, *97*, 071909.
(42) Yoo, J.; Kim, J.-H.; Lee, K.; Lee, S.; Kim, S. S.-W.; Park, H.-K.; Kim, S. S.-W.; Bae, J.; Park, J.-J.; Choi, D. Dewetted Gold Nanoparticles on ZnO Nanorods for Three-Dimensionally Distributed Plasmonic Hot Spots. *Scr. Mater.* **2013**, *69*, 654−657.
(43) Narayanan, R.; Deepa, M.; Srivastava, A. K.; Shivaprasad, S. M. Efficient Plasmonic Dye-Sensitized Solar Cells with Fluorescent Au-Encapsulated C-Dots. *ChemPhysChem* **2014**, *15*, 1106−1115.
(44) Cheng, C. W.; Sie, E. J.; Liu, B.; Huan, C. H. A.; Sum, T. C.; Sun, H. D.; Fan, H. J. Surface Plasmon Enhanced Band Edge Luminescence of ZnO Nanorods by Capping Au Nanoparticles. *Appl. Phys. Lett.* **2010**, *96*, 071107.
(45) Kim, J.; Jeong, Y.; Sohn, Y.; Kang, J. Synthesis and Photophysical Properties of an Eu(II)-Complex/PS Blend: Role of Ag Nanoparticles in Surface-Enhanced Luminescence. *Langmuir* **2012**, *28*, 9842−9848.
(46) Nishimura, F.; Kim, J.-H.; Yonezawa, S.; Takashima, M. Auger Electron Spectroscopy for Chemical State and Quantitative Analysis of Terbium Containing Oxide Fluoride Glasses. *J. Fluorine Chem.* **2014**, *160*, 52−56.
(47) Carnall, W. T.; Fields, P. R.; Rajnak, K. Electronic Energy Levels of the Trivalent Lanthanide Aquo Ions. III. Tb^{3+}. *J. Chem. Phys.* **1968**, *49*, 4447.
(48) Appavoo, K.; Liu, M.; Sfeir, M. Y. Role of Size and Defects in Ultrafast Broadband Emission Dynamics of ZnO Nanostructures. *Appl. Phys. Lett.* **2014**, *104*, 133101.
(49) Stein, G.; Würzberg, E. Energy Gap Law in the Solvent Isotope Effect on Radiationless Transitions of Rare Earth Ions. *J. Chem. Phys.* **1975**, *62*, 208−213.

DOI: 10.1021/acs.langmuir.8b01238
Langmuir 2018, 34, 9774−9780